Viscosity of bubbly magmas from torsional experiments on pumice

Gaetano Ferrante[a], Helge Gonnermann[a], Celine Fliedner[a,b], Thomas Giachetti[c], Amy G. Ryan[a]

[a]Department of Earth, Environmental and Planetary Sciences, Rice University, 6100 Main St, Houston, 77005, TX, USA

[b]TotalEnergies S.E., Avenue Larribau, Pau, 64018, France

[c]Department of Earth Sciences, University of Oregon, 1585 E 13th Ave, Eugene, 97403, OR, USA

Viscosity of bubbly magmas from torsional experiments on pumice

Gaetano Ferrante[a,*], Helge Gonnermann[a], Céline Fliedner[a,b], Thomas Giachetti[c], Amy G. Ryan[a]

[a]*Department of Earth, Environmental and Planetary Sciences, Rice University, 6100 Main St, Houston, 77005, TX, USA*
[b]*TotalEnergies S.E., Avenue Larribau, Pau, 64018, France*
[c]*Department of Earth Sciences, University of Oregon, 1585 E 13th Ave, Eugene, 97403, OR, USA*

Abstract

Bubbles in magma affect its viscosity, one of the most important properties for modeling volcanic eruptions. We performed new viscosity measurements on rhyolitic magma with bubble volume fractions, ϕ, between 0.15 and 0.80. Pumice samples from Medicine Lake Volcano, California, were deformed in torsion-compression experiments at a temperature of 975 °C, and strains up to ∼3. Capillary numbers during the experiments were large and viscosity, η, decreased with increasing ϕ. The experiments have coherent trends in η vs. ϕ with little scatter. We define a new constitutive relation for the relative viscosity of bubbly rhyolitic melt, $\eta_r = \exp[5.5\,\phi/(2-\phi)]$, and for bubbly suspensions at high Capillary numbers in general, reducing the uncertainties associated with scatter among the the body of prior experiments. Our results are useful for more robust modeling of volcanic eruptions.

Keywords: Rheology, suspension, porosity, compaction, relative viscosity, constitutive equation

1. Introduction

The fluid dynamics and ensuing style of a volcanic eruption is largely determined by the viscosity of its magmas. A quantitative knowledge of the factors contributing to variations in magma viscosity is therefore crucial to a more robust understanding of volcanic eruptions. Magma viscosity depends on three contributing factors: (i) the viscosity of the silicate melt, which depends on composition, temperature and potentially on strain rate, if the latter is sufficiently large (Simmons, 1998; Webb and Dingwell, 1990); (ii) the presence of crystals, which may not be present in appreciable quantities or may be present at such high concentrations that their interactions dominate magma viscosity (Lejeune and Richet, 1995; Costa, 2005); and (iii) the presence of bubbles, which are ubiquitous in all magmas (Manga et al., 1998; Llewellin et al., 2002b). Bubbles can either increase or decrease magma viscosity, primarily depending on the balance between the viscous stresses that deform the bubbles and surface tension which acts to restore their sphericity (Rust and Manga, 2002; Stein and Spera, 2002). This force balance is quantified by the Capillary number:

$$Ca = \frac{a\eta_0\dot{\gamma}}{\Gamma}, \qquad (1)$$

where a is the undeformed bubble radius, η_0 is the suspending melt viscosity, $\dot{\gamma}$ is the shear rate and Γ is the surface tension. For Capillary numbers greater than 1, the viscosity of the bubbly mixture is smaller than the viscosity of the melt phase (Rust and Manga, 2002; Stein and Spera, 2002; Llewellin et al., 2002b; Llewellin and Manga, 2005; Mader et al., 2013). This is the case for a wide range of conditions during ascent and eruption of silicic magmas (Llewellin et al., 2002a; Rust et al., 2003).

The essence of the aforementioned effects of bubbles on volcanic eruptions is the reduction in viscous drag on the erupting magma, as a consequence of the decrease in magma viscosity. This can translate to significant effects on magma fragmentation and eruption rate, as suggested by numerical models. For example, accounting for the effect of bubbles on magma viscosity can result in decreases in predicted fragmentation depth of at least 800 m, and 40 to 250% increase in eruption rate, depending on the rheological model used (Llewellin and Manga, 2005; Starostin et al., 2005). Any quantitative assessment of eruptive dynamics therefore requires a sound understanding of the effect of bubbles on magma rheology. Thus, one seeks a robust constitutive
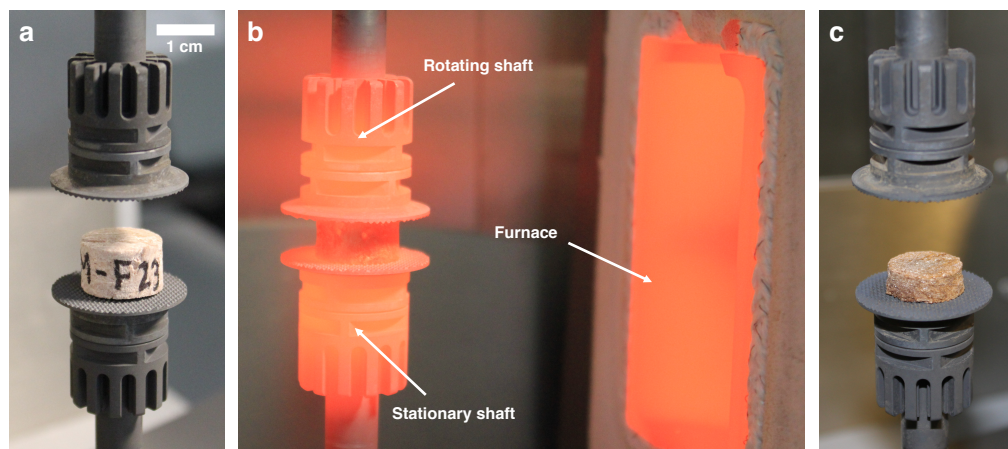
Figure 1: Illustrative example of a sample (BGM-F23) before (**a**), during (**b**), and after (**c**) an experiment. The sample lies between the stationary lower shaft and the rotating upper shaft. The high-temperature furnace is shown to the right of panel b. The post-deformation photo was taken after cooling and retraction of the sample. The change in color between the undeformed sample (**a**) and the deformed sample (**c**) is due to oxidation. Each plate is 2.5 cm in diameter.

relation between the volume fraction of bubbles ϕ and its effect on viscosity, based on experimental measurements of the viscosity of bubbly magmas. Such measurements are challenging because they require high temperatures and well-characterized starting materials. As a consequence, experimentalists have frequently resorted to the use of analog materials under dynamically similar conditions (Rust and Manga, 2002; Llewellin et al., 2002b), including sintered glass particles with integranular porosity (Rahaman et al., 1987; Rahaman and De Jonghe, 1990; Ducamp and Raj, 1989; Sura and Panda, 1990; Quane and Russell, 2005; Quane et al., 2009), in order to complement the relatively modest body of experiments using magmatic melts with bubbles (Bagdassarov and Dingwell, 1992; Lejeune et al., 1999; Stein and Spera, 2002; Vona et al., 2016; Sicola et al., 2021).

Experiments using analog materials, such as bubbly syrups, have been limited in ϕ to values smaller than found in many pyroclasts from explosive eruptions, where the effect of bubbles may be significant. By the same token, the body of experiments using bubbly magmatic melts or sintered glasses encompasses considerable scatter in the data, leaving commensurate uncertainty in the constitutive relation between viscosity and ϕ that have been proposed. To improve upon this current state we have conducted a suite of torsion-compression experiments on rhyolitic melts with bubbles. The principal novelty of our work is that each experiment yields a coherent sequence of viscosity measurements across a wide range of ϕ ($0.15 < \phi < 0.8$). The result is an unequivocal constitutive relation between viscosity and bubble volume fraction with a well-constrained asymptotic value for magma viscosity at high ϕ.

2. Materials and methods

2.1. The samples

We deformed 19 samples of rhyolitic pumice cored from clasts from the Plinian fallout of the 1060 CE Glass Mountain flow of Medicine Lake volcano, California (Heiken, 1978; Giachetti et al., 2015; Gonnermann et al., 2017). The samples are rhyolitic in composition, with SiO_2 content of approximately 72-75 wt% (Table 1; Heiken, 1978) and 0.2-0.5 wt% of magmatic water (Giachetti et al., 2015), texturally homogeneous and mainly phenocryst-poor or free ($< 5\%$; Heiken, 1978). Depending on the size of the clast, one or several cores were drilled and then cut, resulting in 19 samples with diameters ranging from 13.8 to 15.1 mm, and lengths between 7 and 11.5 mm (Figure 1a).

The initial volume fraction of vesicles (i.e. bubbles preserved in the solidified pumice) of our samples ranged between 0.68 and 0.80. Thin sections and scanning electron microscope (SEM) images were produced for a representative sample with vesicularity of 0.75 and vesicle size distributions were obtained by image analysis (Figure 2; Gonnermann et al., 2017). The average vesicle radius is $a_{10} = 4\,\mu m$, at a vesicle number density of $10^{14.6}$ m^{-3}. On the other hand, the volume averaged
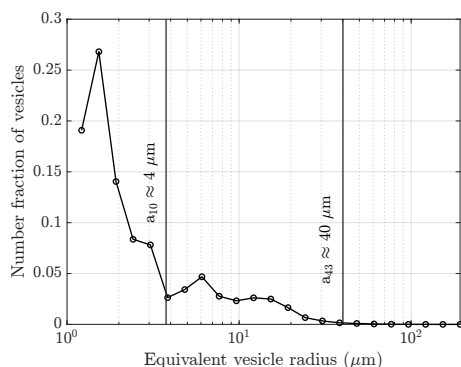
2

Figure 2: Vesicle size distribution of a typical pumice from the Glass Mountain eruption Gonnermann et al. (2017), indicating the arithmentic mean ($a_{10} \approx 4\,\mu m$) and the De Brouckere mean radius ($a_{43} \approx 40\,\mu m$).

(De Brouckere) radius is $a_{43} = 40\,\mu m$. These properties are comparable to Plinian pumices from other eruptions (e.g., Klug et al., 2002; Rust and Cashman, 2011).

Post-deformation scans of representative samples were performed at the High-Resolution X-ray Computed Tomography Facility, University of Texas, Austin, to observe sample microstructure. The scans were obtained at a resolution of 8.7 μm per voxel, at 100 kV, 10 W, and with a 4 s acquisition time, producing a stack of 440–550 regularly spaced images per sample. The latter were then analyzed using the ImageJ software.

2.2. The experiments

The samples were mounted between two parallel plates inside a temperature-controlled oven (Figure 1b), where they were heated to a constant experimental temperature of 975 °C. The parallel plates used in our experiments are serrated to increase grip on the sample and to avoid slip (Figures 1 and S9). Before commencement of the experiments, the samples were held at the experimental temperature for longer than the characteristic thermal diffusion time (~ 100 s), to ensure thermal equilibration. The serrated plates were attached via a shaft to an Anton Paar Physica MCR301 rheometer. Samples were deformed under combined axial and torsional forces. A constant normal force of $F = 2$ N was applied throughout the experiments. Concurrently, a constant torque of $M = 0.0107$ N m was applied for durations of 10 to 300 minutes, depending on the experiment. Details on the individual experiments are provided in Table 1.

Normal force F, torque M, deflection angle θ, rotation rate n, and sample height L were measured by the rheometer. Axial strain ε, shear strain γ, shear stress σ, shear rate $\dot{\gamma}$ and apparent mixture viscosity η were then calculated from the measured quantities (see Table 2 for a list of all the symbols employed in this work).

2.3. Calculated quantities

The axial strain ε experienced by the samples was calculated as

$$\varepsilon = \frac{L - L_{\mathrm{i}}}{L_{\mathrm{i}}}, \tag{2}$$

where L_{i} is the initial length of the samples. In the parallel plate geometry, the shear strain γ and shear rate $\dot{\gamma}$ vary linearly with radial position r as

$$\gamma = \frac{\theta r}{L} \quad \text{and} \quad \dot{\gamma} = \frac{2\pi n r}{L}, \tag{3}$$

respectively, where θ is the cumulative deflection angle at a given time t during the experiment, L and n are the instantaneous length and rotational speed at time t. The distribution of shear stresses σ with radial position for non-Newtonian fluids is, however, not linear. Assuming a power-law fluid, we have

$$\sigma = K\dot{\gamma}^{m}, \tag{4}$$

where K is a material constant and m is the power-law index. K and m are now known a priori. However, the shear viscosity of the fluid in the parallel plate geometry can still be calculated using the "single-point correction" (Figure S6; e.g., Carvalho et al., 1994). The latter relies on the fact that the shear stress corresponding to a non-Newtonian fluid is equal to that associated with a Newtonian fluid at some radial coordinate r_s. For most power-law fluids, $0.75 \leq r_s \leq 0.785$ (Carvalho et al., 1994). Because the shear stress at the sample rim for a Newtonian fluid is known and equal to (e.g., Mezger et al., 2012)

$$\sigma_0(R) = \frac{2M}{\pi R^3}, \tag{5}$$

it follows that the shear stress at $r = r_s$ can be calculated as

$$\sigma(r_s) = \sigma_0(R)\frac{r_s}{R} \tag{6}$$

for a non-Newtonian fluid.

The apparent mixture viscosity calculated at $r = r_s$ is thus given by

$$\eta(r_s) = \frac{\sigma(r_s)}{\dot{\gamma}(r_s)} = \frac{2ML}{2\pi^2 nR^4}. \tag{7}$$

For the usual range of power-law indices m ($0 \leq m \leq 1.2$), encompassing the expected values for bubbly fluids (e.g., Pistone et al., 2016), the viscosity calculated

3

Table 1: Deformation data for the experimental pumice samples. Subscripts i and f denote values at the beginning and at the end of the experiments, respectively. The representative composition (wt%) of BGM rhyolite from Medicine Lake volcano, California is (Giachetti et al., 2015): SiO_2 (74.90), TiO_2 (0.26), Al_2O_3 (14.24), FeO (1.74), MnO (0.04), MgO (0.29), CaO (1.30), Na_2O (3.82), K_2O (4.32), P_2O_5 (0.03).

Sample ID	$\log_{10} \dot{\gamma}_i$ (s^{-1})	$\log_{10} \dot{\gamma}_f$ (s^{-1})	R_i (mm)	R_f (mm)	L_i (mm)	L_f (mm)	ϕ_i	ϕ_f
BGM-F1	-3.23	-3.88	7.00	5.89	9.42	6.90	0.62	0.31
BGM-F10	-2.91	-3.04	7.30	6.87	8.61	6.98	0.77	0.71
BGM-F16	-3.19	-4.12	7.54	6.69	11.52	5.21	0.72	0.24
BGM-F18-1	-2.99	-3.19	7.57	6.40	6.97	5.05	0.67	0.47
BGM-F22	-3.28	-4.20	7.48	6.67	11.42	5.70	0.67	0.16
BGM-F23	-3.27	-3.48	7.49	6.99	9.49	7.92	0.69	0.60
BGM-F3	-3.10	-3.38	7.09	6.34	10.22	8.85	0.71	0.62
BGM-F30-1	-3.30	-3.70	7.51	7.03	7.06	5.60	0.73	0.63
BGM-F4	-3.18	-4.05	7.05	6.48	10.44	5.99	0.72	0.41
BGM-F5-1	-3.03	-3.16	7.27	6.79	8.56	6.68	0.76	0.67
BGM-F5-2	-2.74	-3.26	7.35	6.84	8.08	5.23	0.76	0.58
BGM-F6	-3.04	-3.93	7.25	6.36	8.69	5.16	0.71	0.33
BGM-F8	-3.20	-3.73	7.35	6.54	9.79	6.23	0.71	0.46
BGM-F9-1	-3.08	-3.46	7.36	6.81	9.18	6.88	0.72	0.58
BGM-G10	-3.11	-3.96	6.95	5.99	10.26	5.36	0.76	0.36
BGM-G12	-2.78	-3.37	6.90	5.67	10.31	4.97	0.83	0.51
BGM-G2	-3.01	-3.49	6.88	6.28	10.03	6.90	0.72	0.52
BGM-G7	-3.12	-3.81	7.30	6.57	10.78	6.07	0.71	0.36
BGM-G8	-3.23	-3.95	7.17	6.28	10.00	6.02	0.68	0.33

via single point correction at $r = r_s = 0.755$ is within 1% of the true value (Carvalho et al., 1994).

We calculate the variables of interest (namely shear strain γ, shear rate $\dot{\gamma}$, shear stress σ and apparent viscosity η) for $r = r_s$. All four variables depend on both the radius of the sample and the gap between the plates. The latter is measured by the rheometer throughout the experiment. The sample radius is, however, measured only at the beginning and at the end of each experiment. The time-dependent sample radius is calculated with the method described in Section S2. However, since the changes in sample radius during the experiments are relatively small compared to the changes in the other controlling variables (Table 1), variations in sample radius arising from uncertainty in its estimate do not produce noticeable changes in results.

Bubble volume fraction of each sample over the course of the experiment was calculated using (i) L, the measured height of the cylindrical sample; (ii) the time-dependent sample radius R (Section S2); (iii) mass M_t of the samples, measured using a precision scale; (iv) the average density of the sample matrix $\rho_m = 2430 \, \text{kg m}^{-3}$, determined by He-pycnometry (Giachetti et al., 2015). The sample radius and length were used to calculate the envelope volume V_t of each sample throughout the experiments. The matrix volume of each sample was then calculated as $V_m = M_t/\rho_m$, and the bubble volume fraction as $\phi = (V_t - V_m)/V_t$.

3. Results

3.1. Deformation data

The gap between the plates L, the deflection angle of the upper plate θ and its rotation rate n are shown in Figure 3. Shear stress σ, shear rate $\dot{\gamma}$ and shear strain γ were calculated from the raw measurements following the methods outlined in Section 2.3. The results calculated at the single point radius $r = r_s \approx 0.755R$ are shown in Figure 4. It is worth noting that since shear strain and shear rate increase linearly with increasing distance from the rotation axis, their values at $r = r_s$ are a factor 0.755 smaller than the maximum values at the sample rim and shown in Figure S7

Although the samples are subjected to a constant torque of $M = 0.0107 \, \text{N m}$, shear stresses at $r = r_s$ range from 12 kPa to 25 kPa over the course of each experiment time (Figure 4a) because of the change in sample radius (Figure S5). The resulting shear rates range from $10^{-4.35} \, \text{s}^{-1}$ to $10^{-2.86} \, \text{s}^{-1}$ (Figure 4b). At all times during the experiments the Capillary number was greater than 1 (Section S1), and the shear rates were below the onset of non-Newtonian melt behavior (Figure S8; Webb and Dingwell, 1990). Shear rate exhibits random fluctuations about the average rate, resulting from fluctuations
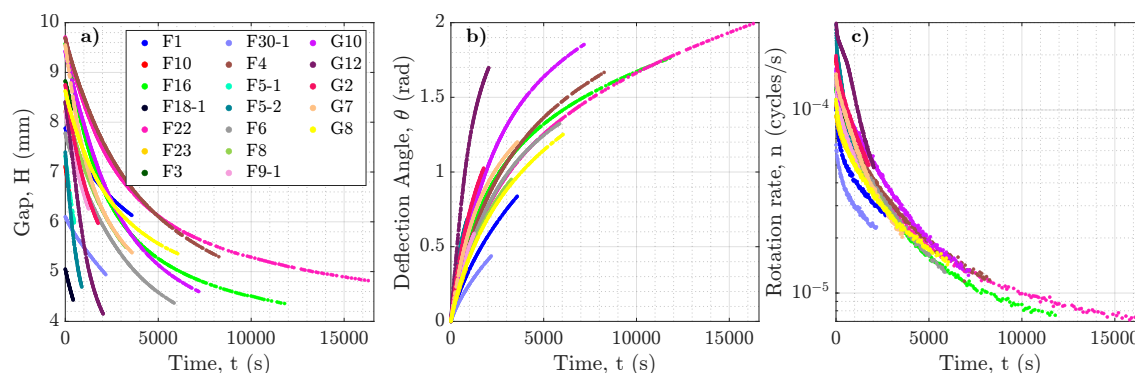
4

Figure 3: Raw mechanical data: gap between the plates (**a**), deflection angle (**b**) and rotation rate of the upper plate (**c**) as a function of time.

Symbol	Description	Unit
a_{10}	Average vesicle radius	m
a_{43}	De Brouckere vesicle radius	m
F	Normal force	N
K	Power-law fluid constant	Pa s^m
L	Sample length	m
M	Torque	N m
m	Power-law fluid index	-
n	Plate rotation rate	s^{-1}
r	Sample radial coordinate	m
r_s	Single-point radial coordinate	m
R	Sample radius	m
T	Temperature	°C
V_m	Sample matrix volume	m^3
V_t	Sample envelope volume	m^3
α	Fitting parameter	-
γ	Shear strain	-
$\dot{\gamma}$	Shear rate	s^{-1}
ε	Axial strain	-
η	Mixture viscosity	Pa s^{-1}
η_r	Relative viscosity	Pa s^{-1}
η_0	Suspending melt viscosity	Pa s^{-1}
θ	Plate deflection angle	rad
ϕ	Bubble volume fraction	-
ϕ_a	ϕ at viscosity asymptote	-
ρ_m	Sample matrix density	kg m^{-3}
σ	Shear stress	Pa
ω	Plate rotational speed	rad s^{-1}

Table 2: List of symbols employed in this study with description and unit.

in measured rotation rate (Figures 3c and S11). We do not know whether they represent actual small variations in sample deformation rate or whether they are associated with minor slippage. The variability in rotation rate is of ±2% about the average rate, resulting in an estimated uncertainty in our shear viscosity calculations of approximately 2%.

Over the course of a given experiment γ increases due to the imposed shear deformation, reaching final values between $\gamma = 0.15$ and $\gamma = 2$ (Figure 4c, inset). Concurrently, because of the axial force, samples undergo compaction (e.g., Ashwell et al., 2015), that is the volume fraction of bubbles ϕ decreases during the experiment (Figure 4d), reaching axial strains between $\varepsilon = 0.05$ and $\varepsilon = 0.55$ (Figure 4e). As a consequence of the decrease in ϕ, shear rates decrease (Figure 4b), and the apparent mixture viscosity η increases over the course of the experiments (Figure 4f). Viscosities calculated in shear are compared to those calculated from the shortening of the samples in Figure S3. The two viscosities are comparable and correlate with each other, showing no systematic trend that would indicate that viscosities calculated from rotation (shear) rate are biased by slippage of the upper or lower plates. Moreover, because the deformation rate resulting from the shortening of the sample is on average one order of magnitude smaller than the shear rate, this analysis substantiates our estimates of high Capillary number.

Permeability of the samples was measured before and after each experiment (see Gonnermann et al., 2017). All samples were permeable to begin with. Although permeability decreased with strain, it remained sufficiently large for compaction to occur throughout the experiments (Figure 4d). Thus, unlike similar experiments by Okumura et al. (2013) on foamed obsidian, there was no strain limit associated with the onset of compaction
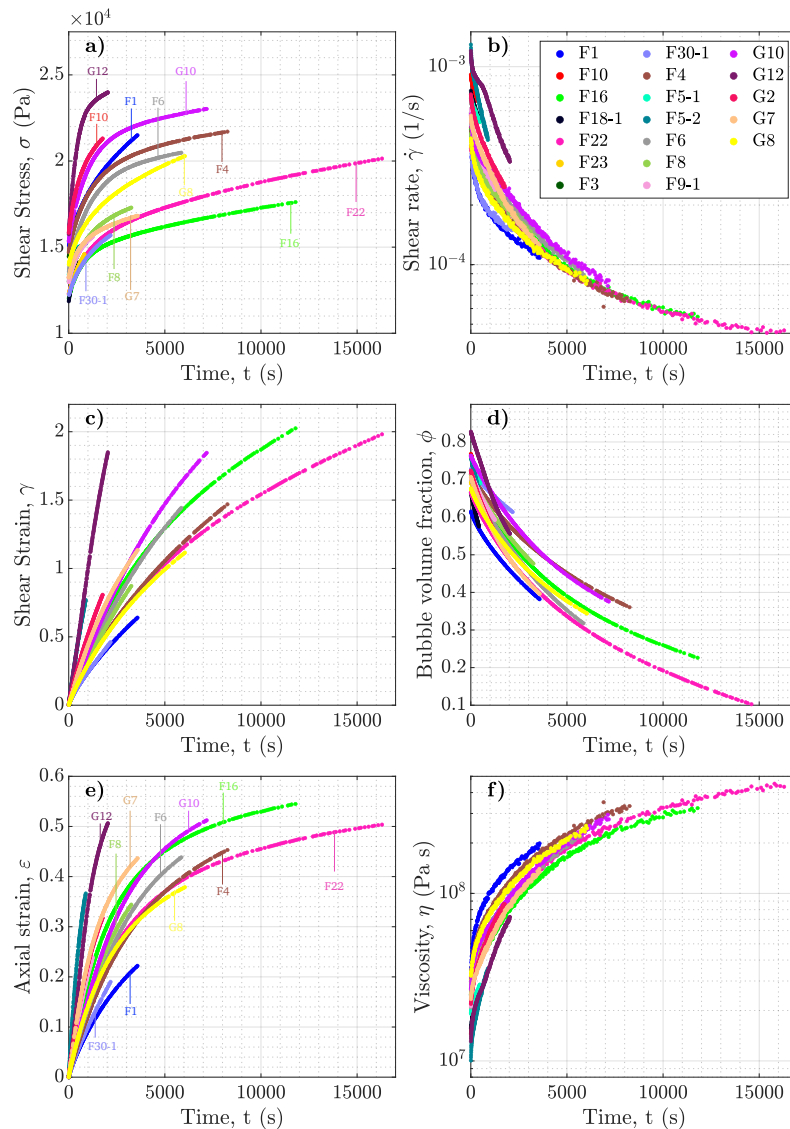
5

Figure 4: Mechanical data for each experiment calculated at $r = r_s$ (i.e. the radial coordinate corresponding to the single point correction). Each point in every curve represents one individual measurement. **a:** Shear stress σ as a function of time t. **b:** Shear rate $\dot{\gamma}$ as a function of time t. **c:** Shear strain γ as a function of time t. **d:** Bubble volume fraction ϕ as a function of time t. **e:** Axial strain ε as a function of time t. **f:** Viscosity η as a function of time t.

in our experiments, because our pumice samples were already permeable. During deformation, the samples were at all times in contact with the plates (Figures 1 and S9a). Deformation of the samples was uniformly distributed along their height (Figures 5, 6 and S9). Some samples, however, exhibit densification within a zone near their center in the axial direction (Figures 5 and S13). Since the samples are heterogeneous to begin with, the latter could be attributed to initial variability in vesicularity across the sample. However, we cannot rule out the occurrence of some degree of concentration of shear deformation near the center of some samples. This has not been accounted for in our analysis. However, no evidence of fracturing or shear localiza-
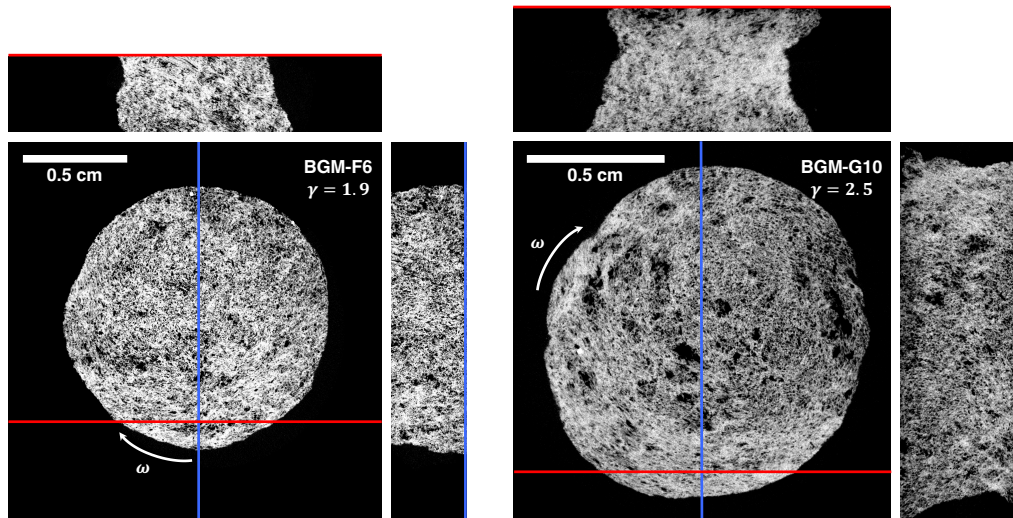
6

Figure 5: Post-deformation computed microtomography scans of two representative samples (BGM-F6 and BGM-G10), showing transverse, longitudinal axial and longitudinal tangential sections.

tion along weak planes was observed (Figure 5), consistent with the high-temperature experiments by Okumura et al. (2013). Because shear strain and shear rate in the samples increase linearly along the radial coordinate, computed microtomography scans provide observations of deformation across a wide range of shear strains and shear rates, showing increasing bubble elongation and alignment with increasing distance from the rotation axis (Figure 5). A close-up of the longitudinal tangential section of representative sample BGM-F6 taken at $r \approx r_s$ is provided in Figure 6, showing alignment and deformation of bubbles at the shear rates of interest for our viscosity calculations.

3.2. Sampling of the data

All experiments exhibit a steep drop in shear rate at the beginning of the experiment (Figure 7), which is thought to be a consequence of sample loading. These 'loading' periods are typically not used for analysis. Instead, one uses the data during which shear rates decrease more steadily, as shown by the linear decrease in $\log \dot{\gamma}$ with increasing γ signaled by the large dots in Figure 4f. Following this conventional approach to avoid transient rheological effects associated with small strains (Manga and Loewenberg, 2001; Stein and Spera, 2002), we excluded the initial loading period in our analysis and subsequent figures.

3.3. Functional relation between viscosity and volume fraction of bubbles

Our data constitute a continuous sequence of viscosity measurements across a range of bubble volume fractions from 0.16 to 0.76. The apparent viscosity, η, increases with decreasing bubble volume fraction, ϕ (Figure 8). This is consistent with previous experiments on silicate melts at large Capillary numbers (Bagdassarov and Dingwell, 1992; Lejeune et al., 1999; Stein and Spera, 2002). For all samples there is a similar trend in η as a function of ϕ, which overlaps for the majority of samples.

We find that the trend emerging from our data is well represented by a modified version of the constitutive relation proposed by Ducamp and Raj (1989) (Figure 8a):

$$\ln(\eta/\eta_0) = -\alpha\,\phi/(1 + \phi_a - \phi) = -\alpha\,\phi/(2 - \phi). \quad (8)$$

In contrast with Ducamp and Raj's original equation, Equation 8 accounts for the fact that the experimental data $\eta(\phi)$ follows a trend for which η does not go to zero at large ϕ, but rather approaches a finite value at $\phi = \phi_a$ (Figure 8b). For convenience we choose the limit $\phi_a = 1$.

The value of η_0 in Equation 8 is a fitting parameter that is allowed to vary between experiments, while α is a fitting parameter that is constrained to be the same for all experiments. Conceptually, η_0 represents the value of η at $\phi = 0$. For most samples, the fit yields
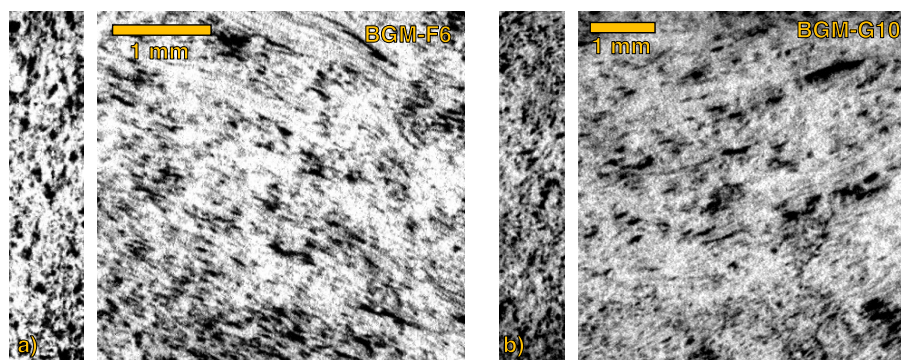
7

Figure 6: Close-ups of post-deformation computed microtomography scans of representative samples BGM-F6 (**a**) and BGM-G10 (**b**), showing undeformed bubbles around the sample rotation axis (left panels), where the shear rates are the lowest, and deformed bubbles close to the sample rim (right panels), where the shear rates are the highest.
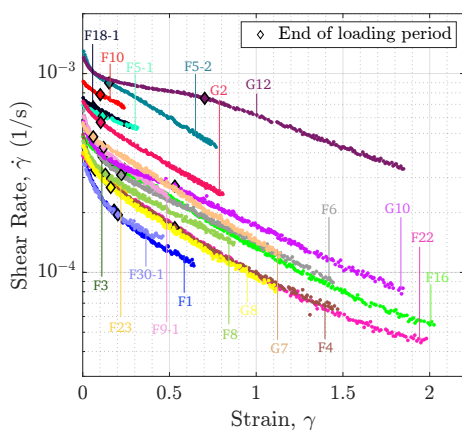

Figure 7: Shear rate log $\dot{\gamma}$ as a function of shear strain γ. The colored diamonds represent our picks for the end of the loading periods, which were excluded from our analysis (see Figure S4 for individual curves).

$\eta_0 \approx 6 \pm 1 \times 10^8$ Pa s. Three samples have values of $\eta_0 \approx 12 \pm 1 \times 10^8$ Pa s, while two samples have values of $\eta_0 \approx 3 \pm 1 \times 10^8$ Pa s. Our fitted values of η_0 fall between the measurements of Webb and Dingwell (1990) and Stevenson et al. (1996) on anhydrous Little Glass Mountain obsidian and hydrous (0.13 wt.% H_2O) Big Glass Mountain obsidian. We attribute the inferred variations in η_0 to potential differences in SiO_2, crystal, and/or microlite content (Stevenson et al., 1996) among the samples.

We define a relative viscosity $\eta_r = \eta/\eta_0$. When plotted as a function of ϕ, it is apparent that all experiments delineate a singular coherent trend (Figure 8c) given by

$$\eta_r = e^{-\alpha\phi/(2-\phi)} \tag{9}$$

with $\alpha = 5.5$ (see Section S2 for details on the model fit). The denominator on the right hand side of Equation 8 implies that for large ϕ the relative viscosity approaches a value of $\eta_r = e^{-\alpha} \approx 0.004$. Conceptually this value represents the high-ϕ limit of η_r for bubbly suspensions at high Capillary numbers. Although in our fitting of the experimental data we have assumed that $\phi_a = 1$, the rheological transition from a wet foam to a dry foam occurs at somewhat lower values of ϕ ($\phi \approx 0.9$; Furuta et al., 2016). To what extent such an asymptotic value of η_r exists in general, and how variable it is between bubbly suspension of different types, is unclear. Here the limit $\eta_r \approx 0.004$ has the role of preventing the constitutive equation from predicting unrealistic values of η_r when $\phi \to 1$. Our data does not extend to such high values of ϕ and the smallest value of η_r realized in our experiments is ≈ 0.04. The trend of the data, if extrapolated, suggests that η_r does decrease further with increasing ϕ, but it is unclear up to what

8

limit. These nuances aside, our data provide a remarkably coherent trend that enables us to provide a well-constrained constitutive model for η_r over a range in ϕ that encompasses most of what may be expected during rhyolitic eruptions, based on the volume fraction of vesicles measured in volcanic samples (Houghton and Wilson, 1989; Klug et al., 2002; Carey et al., 2009; Alfano et al., 2012).

4. Discussion

4.1. Comparison with previous experimental studies

Previously published experiments on the rheology of bubbly melts at high Capillary number are listed in Table A1 and shown in Figure 9. Starting materials include vesicular melts (light blue symbols in Figure 9; Bagdassarov and Dingwell, 1992; Lejeune et al., 1999; Stein and Spera, 2002; Okumura et al., 2013; Vona et al., 2016; Sicola et al., 2021) and sintered particles, such as glass powders (empty gray symbols; Rahaman et al., 1987; Ducamp and Raj, 1989; Sura and Panda, 1990; Rahaman and De Jonghe, 1990; Quane and Russell, 2005) and volcanic ash (filled gray symbols; Quane et al., 2009; Heap et al., 2014).

Only six data points are available in the literature for bubble volume fractions greater than 0.6, with a maximum of 0.68 (Bagdassarov and Dingwell, 1992), which is from vesiculated rhyolitic obsidian. Our experiments are the first to be conducted on naturally occurring pumiceous pyroclasts, which allowed us to reach bubble volume fractions as high as 0.76, while maintaining the realism associated with natural compositions and bubble size distributions. Most experiments have been conducted under uniaxial loading, although Stein and Spera (2002) employed a concentric cylinder geometry, and Okumura et al. (2013) used a torsion apparatus. Our torsion-compression geometry allowed us to reach shear strains as high as 2.8.

When shown in terms of the relative viscosity, η_r, our results are in good agreement with those of Stein and Spera (2002) (performed on vesicular rhyolite), Ducamp and Raj (1989), Rahaman and De Jonghe (1990) (both performed on sintered glass particles) and Quane et al. (2009) (performed on sintered rhyolitic ash). For bubble volume fractions lower than 0.35, our results are also in excellent agreement with experiments performed by Sicola et al. (2021) on foamed rhyolite with fluid-filled bubbles (labeled "single stage" in Figure 9), but the two datasets significantly diverge for $\phi > 0.4$. However, while some of the existing studies fall on or near our data, scatter amongst the published measurements is too large to establish a definite relationship between η_r and ϕ. Our measurements not only augment the existing body of published data, but also support the new constitutive relation provided by Equation 8, which also provides a good fit to the experimental data of Stein and Spera (2002); Ducamp and Raj (1989); Rahaman and De Jonghe (1990); Quane et al. (2009).

4.2. Comparison with previous models

Figure 9 shows that previously proposed models for $\eta_r(\phi)$ of Manga and Loewenberg (2001), Pal (2003), Rust and Manga (2002), Bagdassarov and Dingwell (1992), and Ducamp and Raj (1989) do not fit our data.

The model of Manga and Loewenberg (2001) is based on numerical simulations of bubble deformation in simple shear flow and their results consistently overestimate η_r for $0 < \phi < 0.4$.

Pal (2003) proposed four theoretical models for the relative viscosity of concentrated bubbly suspensions. Among the four models, their "model 2" is the most widely used in volcanology and commonly referred to as the *minimum model* (Llewellin and Manga, 2005). For large capillary numbers, their model yields

$$\eta_r = (1 - \phi)^{5/3} \qquad (10)$$

and consistently overestimates η_r.

Rust and Manga (2002) performed concentric cylinder experiments on dilute suspensions of bubbles in corn syrup at Capillary numbers of order 1. They fitted the Cross (1965) model to their data, assuming the Krieger and Dougherty (1959) equation as the high capillary number limit of η_r to obtain

$$\eta_r = \left(1 - \frac{\phi}{\phi_m}\right)^{2.37\phi_m}, \qquad (11)$$

with $\phi_m = 0.9$. For bubble volume fractions lower than 0.65, Equation 11 is in excellent agreement with our results. However, for ϕ greater than 0.7 it significantly under-predicts η_r from our experiments. Given that the experiments upon which Equation 11 is based are at Capillary numbers ~ 1 and for $\phi < 0.2$, this divergence is not surprising.

In contrast to the aforementioned constitutive models, Bagdassarov and Dingwell (1992) performed parallel plate viscometry experiments on vesicular rhyolite to obtain the empirical relation

$$\eta_r = \frac{1}{1 + C\phi}, \qquad (12)$$

where $C = 22.4$. Equation 12 is commonly referred in the literature as the *maximum model* for the effect
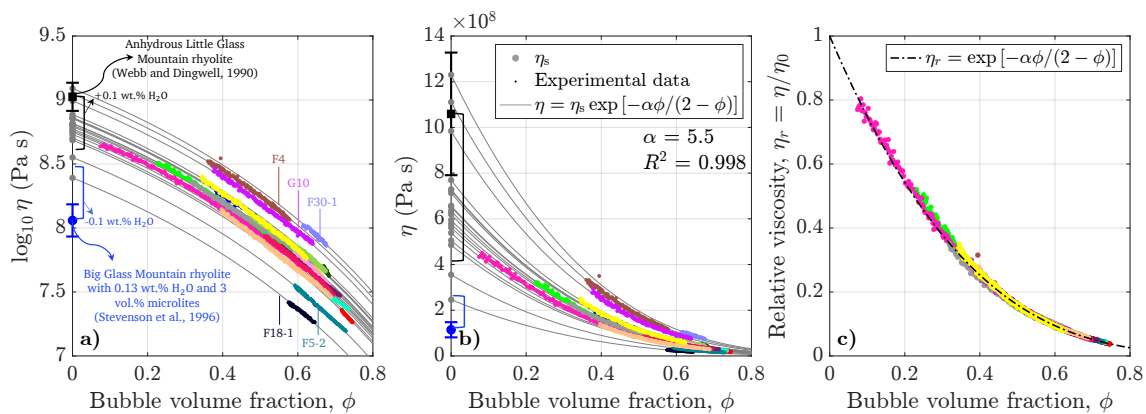
9

Figure 8: Experimental data of apparent viscosity as a function of bubble volume fraction. Thin gray lines represent model fits to the experimental data. Gray dots on the y axis represent the bubble-free melt viscosity η_0 for each sample. Different colors represent different experiments. The black square and the blue circle represent viscosity measurements of Little Glass Mountain (Webb and Dingwell, 1990) and Big Glass Mountain (Stevenson et al., 1996) rhyolites, respectively. The corresponding effects of water content on viscosity are estimated with the model of Giordano et al. (2008). **a:** Logarithm of apparent mixture viscosity, $\log_{10} \eta$, as a function of bubble volume fraction, ϕ. **b:** Apparent mixture viscosity, η, as a function of bubble volume fraction, ϕ. **c:** Relative viscosity, η_r, as a function of bubble volume fraction, ϕ.
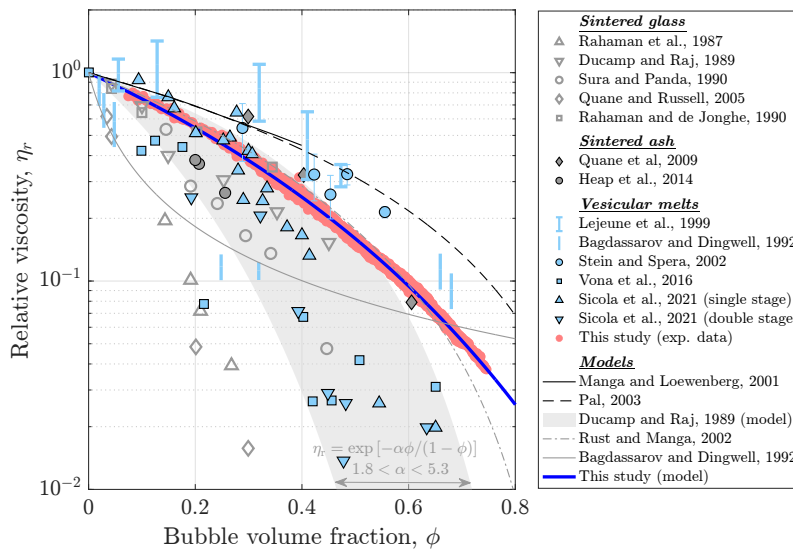

Figure 9: Relative viscosity η_r as a function of bubble volume fraction ϕ for previous works and for the present study. Light blue symbols represent previous studies conducted on vesicular melts, while gray symbols represent previous studies conducted on sintered particles, including glass (open symbols) and volcanic ash (filled symbols). Theoretical models are shown as black lines, while empirical model are shown in gray. The results of the present study are shown as the red dots (data) and the blue line (model).

of bubbles on magma viscosity (Llewellin and Manga, 2005). This model differs significantly from other models in that η_r decreases very rapidly for $\phi < 0.1$, but showcases virtually no change in the range $0.2 < \phi < 0.7$.

Ducamp and Raj (1989) proposed an empirical relation based on experiments on porous glasses, given by

$$\eta_r = \exp\left(-\alpha \frac{\phi}{1-\phi}\right), \qquad (13)$$

where α is an adjustable parameter. For small porosities, their model reduces to the exact solution of Macken-zie (1950), obtained for dilute suspensions of spherical

10

pores

$$\eta_r = (1 - \alpha\phi), \qquad (14)$$

with $\alpha = 5/3$ in the derivation of Mackenzie (1950). The model proposed by Ducamp and Raj (1989) generalizes Equation 14 to non-dilute suspensions of arbitrarily shaped pores. It has been used to model relative viscosity as a function of bubble volume fraction for vesicular melts and sintered particles with intergranular porosity, with the objective of moving towards a general constitutive equation for materials of volcanological interest (Quane and Russell, 2005; Quane et al., 2009; Heap et al., 2014; Vona et al., 2016; Sicola et al., 2021). A wide range of values for the parameter α have been obtained by fitting experimental data to Equation 13 (Table A1), as shown by the shaded gray area in Figure 9. While Equation 13 provides a good fit at small ϕ, the exponential decrease of η_r at high ϕ diverges significantly from our experimental data, motivating our modification of Ducamp and Raj's model provided by our Equation 8.

5. Conclusion

Magma eruption rate is a consequence of the dynamical balance between driving forces during eruptive magma ascent (buoyancy and excess pressure) and resistive viscous forces. The latter requires a robust constitutive model for the effect of bubbles on magma viscosity. The experimental data presented herein reduce prior uncertainty in the functional relation between apparent viscosity of silicic bubbly magma and its bubble volume fraction. The coherent trend exhibited by our new data leads to a new constitutive relation for apparent viscosity as a function of bubble volume fraction at high Capillary numbers. This new constitutive relation represents a modification of the model proposed by Ducamp and Raj (1989). It includes a limit value for the relative viscosity as bubble volume fraction becomes large, thus avoiding unrealistically low viscosities at high bubble volume fractions.

Declaration of competing interest

The authors declare that they have no known competing financial interests or personal relationships that could have appeared to influence the work reported in this paper.

Data availability

Data will be made available upon request.

Appendix A. Previous studies

References

Alfano, F., Bonadonna, C., Gurioli, L., 2012. Insights into eruption dynamics from textural analysis: the case of the may, 2008, chaitén eruption. Bulletin of Volcanology 74, 2095–2108.

Ashwell, P.A., Kendrick, J.E., Lavallée, Y., Kennedy, B.M., Hess, K.U., von Aulock, F.W., Wadsworth, F.B., Vasseur, J., Dingwell, D.B., 2015. Permeability of compacting porous lavas. Journal of Geophysical Research: Solid Earth 120, 1605–1622.

Bagdassarov, N., Dingwell, D.B., 1992. A rheological investigation of vesicular rhyolite. Journal of volcanology and geothermal research 50, 307–322.

Carey, R., Houghton, B., Thordarson, T., 2009. Abrupt shifts between wet and dry phases of the 1875 eruption of askja volcano: Microscopic evidence for macroscopic dynamics. Journal of Volcanology and Geothermal Research 184, 256–270.

Carvalho, M., Padmanabhan, M., Macosko, C., 1994. Single-point correction for parallel disks rheometry. Journal of Rheology 38, 1925–1936.

Costa, A., 2005. Viscosity of high crystal content melts: dependence on solid fraction. Geophysical Research Letters 32.

Cross, M.M., 1965. Rheology of non-newtonian fluids: a new flow equation for pseudoplastic systems. Journal of colloid science 20, 417–437.

Ducamp, V.C., Raj, R., 1989. Shear and densification of glass powder compacts. Journal of the American Ceramic Society 72, 798–804.

Furuta, Y., Oikawa, N., Kurita, R., 2016. Close relationship between a dry-wet transition and a bubble rearrangement in two-dimensional foam. Scientific reports 6, 37506.

Giachetti, T., Gonnermann, H.M., Gardner, J.E., Shea, T., Gouldstone, A., 2015. Discriminating secondary from magmatic water in rhyolitic matrix-glass of volcanic pyroclasts using thermogravimetric analysis. Geochimica et Cosmochimica Acta 148, 457–476.

Giordano, D., Russell, J.K., Dingwell, D.B., 2008. Viscosity of magmatic liquids: a model. Earth and Planetary Science Letters 271, 123–134.

Gonnermann, H.M., Giachetti, T., Fliedner, C., Nguyen, C.T., Houghton, B.F., Crozier, J.A., Carey, R.J., 2017. Permeability during magma expansion and compaction. Journal of Geophysical Research: Solid Earth 122, 9825–9848.

Heap, M., Kolzenburg, S., Russell, J., Campbell, M., Welles, J., Farquharson, J., Ryan, A., 2014. Conditions and timescales for welding block-and-ash flow deposits. Journal of Volcanology and Geothermal Research 289, 202–209.

Heiken, G., 1978. Plinian-type eruptions in the Medicine Lake Highland, California, and the nature of the underlying magma. Journal of Volcanology and Geothermal Research 4, 375–402.

Houghton, B., Wilson, C., 1989. A vesicularity index for pyroclastic deposits. Bulletin of volcanology 51, 451–462.

Table A1: Compilation of published studies on the effect of vesicularity on the relative viscosity of suspensions (as shown in Figure 9), with the experimental materials and methods employed and the reported α-values obtained by fitting Equation 13 to the data. Values of α reported from fitting $\log_{10}\eta$ (α_{10}) have been converted to their respective value from fitting $\ln\eta$.

Reference	Material	Method	ϕ	T (°C)	α
Rahaman et al. (1987)	Soda-lime glass powder	Uniaxial loading	0.14-0.34	605	-
Ducamp and Raj (1989)	Corning glass powder	Uniaxial loading	0.04-0.45	850	2.5-4
Sura and Panda (1990)	Cordierite glass powder	Uniaxial loading	0.15-0.45	850	-
Rahaman and De Jonghe (1990)	Borosilicate glass powder	Uniaxial loading	0.04-0.34	800	-
Bagdassarov and Dingwell (1992)	Vesiculated rhyolite	Dilatometry	0.02-0.68	849-852	-
Lejeune et al. (1999)	Vesiculated $CaAl_2Si_2O_8$ melts	Uniaxial loading	0.06-0.47	830-960	-
Stein and Spera (2002)	Foamed rhyolite	Concentric cylinder	0.29-0.56	950-1150	-
Quane and Russell (2005)	Sintered soda lime beads	Uniaxial loading	0.03-0.30	535.650	5.3
Quane et al. (2009)	Sintered rhyolitic ash	Uniaxial loading	0.30-0.61	800-900	1.8
Okumura et al. (2013)	Vesiculated rhyolite	Torsion	0.1-0.76	850-960	-
Heap et al. (2014)	Unconsolidated ash and lapilli	Uniaxial loading	0.05-0.25	800-900	4.61
Vona et al. (2016)	Foamed rhyolitic obsidian	Uniaxial loading	0.1-0.65	750	3.39[a]
Sicola et al. (2021)	Foamed rhyolitic obsidian	Dilatometry	0.09-0.65	750-800	2.47
Sicola et al. (2021)	Foamed rhyolitic obsidian	Dilatometry	0.19-0.63	750	3.68
This study	Rhyolitic pumice	Torsion-compression	0.16-0.81	975	5.5[b]

[a]Obtained by fitting $\log_{10}\eta = \log_{10}\eta_0 - \alpha_{10}(\frac{\phi}{1-\phi})^\beta$

[b]Obtained by fitting $\ln\eta = \ln\eta_0 - \alpha(\frac{\phi}{2-\phi})$

Klug, C., Cashman, K., Bacon, C., 2002. Structure and physical characteristics of pumice from the climactic eruption of Mount Mazama (Crater Lake), Oregon. Bulletin of Volcanology 64, 486–501.

Krieger, I.M., Dougherty, T.J., 1959. A mechanism for non-newtonian flow in suspensions of rigid spheres. Trans. Soc. Rheol 3, 137–152.

Lejeune, A., Bottinga, Y., Trull, T., Richet, P., 1999. Rheology of bubble-bearing magmas. Earth and Planetary Science Letters 166, 71–84.

Lejeune, A., Richet, P., 1995. Rheology of crystal-bearing silicate melts: An experimental study at high viscosities. Journal of Geophysical Research: Solid Earth 100, 4215–4229.

Llewellin, E., Mader, H., Wilson, S., 2002a. The constitutive equation and flow dynamics of bubbly magmas. Geophysical research letters 29, 23–1.

Llewellin, E., Mader, H., Wilson, S., 2002b. The rheology of a bubbly liquid. Proceedings of the Royal Society of London. Series A: Mathematical, Physical and Engineering Sciences 458, 987–1016.

Llewellin, E., Manga, M., 2005. Bubble suspension rheology and implications for conduit flow. Journal of Volcanology and Geothermal Research 143, 205–217.

Mackenzie, J., 1950. The elastic constants of a solid containing spherical holes. Proceedings of the Physical Society. Section B 63, 2.

Mader, H., Llewellin, E., Mueller, S., 2013. The rheology of two-phase magmas: A review and analysis. Journal of Volcanology and geothermal Research 257, 135–158.

Manga, M., Castro, J., Cashman, K.V., Loewenberg, M., 1998. Rheology of bubble-bearing magmas. Journal of Volcanology and Geothermal Research 87, 15–28.

Manga, M., Loewenberg, M., 2001. Viscosity of magmas containing highly deformable bubbles. Journal of Volcanology and Geothermal Research 105, 19–24.

Mezger, T.G., et al., 2012. The rheology handbook. volume 10. Vincentz Network Hannover, Germany.

Okumura, S., Nakamura, M., Uesugi, K., Nakano, T., Fujioka, T., 2013. Coupled effect of magma degassing and rheology on silicic volcanism. Earth and Planetary Science Letters 362, 163–170.

Pal, R., 2003. Rheological behavior of bubble-bearing magmas. Earth and Planetary Science Letters 207, 165–179.

Pistone, M., Cordonnier, B., Ulmer, P., Caricchi, L., 2016. Rheological flow laws for multiphase magmas: An empirical approach. Journal of Volcanology and Geothermal Research 321, 158–170.

Quane, S.L., Russell, J., 2005. Welding: insights from high-temperature analogue experiments. Journal of Volcanology and Geothermal Research 142, 67–87.

Quane, S.L., Russell, J.K., Friedlander, E.A., 2009. Time scales of compaction in volcanic systems. Geology 37, 471–474.

Rahaman, M.N., De Jonghe, L.C., 1990. Sintering of spherical glass powder under a uniaxial stress. Journal of the American Ceramic Society 73, 707–712.

Rahaman, M.N., De Jonghe, L.C., Scherer, G.W., Brook, R.J., 1987. Creep and densification during sintering of glass powder compacts. Journal of the American Ceramic Society 70, 766–774.

Rust, A., Cashman, K., 2011. Permeability controls on expansion and size distributions of pyroclasts. Journal of Geophysical Research: Solid Earth 116.

Rust, A., Manga, M., 2002. Effects of bubble deformation on the viscosity of dilute suspensions. Journal of non-newtonian fluid mechanics 104, 53–63.

Rust, A., Manga, M., Cashman, K.V., 2003. Determining flow type, shear rate and shear stress in magmas from bubble shapes and orientations. Journal of Volcanology and Geothermal Research 122, 111–132.

Sicola, S., Vona, A., Ryan, A.G., Russell, J.K., Romano, C., 2021. The effect of pores (fluid-filled vs. drained) on magma rheology. Chemical Geology 569, 120147.

Simmons, J.H., 1998. What is so exciting about non-linear viscous flow in glass, molecular dynamics simulations of brittle fracture and semiconductor–glass quantum composites. Journal of non-crystalline solids 239, 1–15.

12

Starostin, A., Barmin, A., Melnik, O., 2005. A transient model for explosive and phreatomagmatic eruptions. Journal of Volcanology and Geothermal Research 143, 133–151.

Stein, D.J., Spera, F.J., 2002. Shear viscosity of rhyolite-vapor emulsions at magmatic temperatures by concentric cylinder rheometry. Journal of Volcanology and Geothermal Research 113, 243–258.

Stevenson, R.J., Dingwell, D.B., Webb, S.L., Sharp, T.G., 1996. Viscosity of microlite-bearing rhyolitic obsidians: an experimental study. Bulletin of Volcanology 58, 298–309.

Sura, V.M., Panda, P.C., 1990. Viscosity of porous glasses. Journal of the american Ceramic Society 73, 2697–2701.

Vona, A., Ryan, A.G., Russell, J.K., Romano, C., 2016. Models for viscosity and shear localization in bubble-rich magmas. Earth and Planetary Science Letters 449, 26–38.

Webb, S.L., Dingwell, D.B., 1990. Non-newtonian rheology of igneous melts at high stresses and strain rates: Experimental results for rhyolite, andesite, basalt, and nephelinite. Journal of Geophysical Research: Solid Earth 95, 15695–15701.

13